Tribology International 175 (2022) 107846

Contents lists available at ScienceDirect

Tribology International

journal homepage: www.elsevier.com/locate/triboint

Heat effects modelling on the efficiency loss of the lubricating interface between piston and cylinder in axial piston pumps

Gaston Haidak [a], Xiaofeng Wei [a], Feiyue Li [a], Andrews Larbi [a], Dongyun Wang [a,b,*]

[a] Zhejiang Normal University, Jinhua, Zhejiang 321004, China
[b] Key Laboratory of Urban Rail Transit Intelligent Operation and Maintenance Technology & Equipment of Zhejiang Province, Zhejiang 321005, China

ARTICLE INFO

Keywords:
Axial Piston pump
Piston/cylinder interface
Efficiency loss
Thermal effects
Thermoelastohydrodynamic deformation

ABSTRACT

This work presents a systematic analysis of the tribological properties of the lubricant and the thermal exchange effect on the deformation of the solid-fluid structure between the piston and cylinder block in an axial piston pump. A thermo-elastohydrodynamic model is established and used to study the pump. Fluid film properties, friction forces and leakage of the solid-fluid structure are calculated and analysed under normal operating conditions of the axial piston pump s. The friction and leakage losses representing the direct total power loss are analysed for different conditions. Furthermore, the thermal effects on the oil film properties and lubrication mechanisms are calculated and discussed. This work provides sufficient methods and processes to evaluate the causes of the lubrication failure. It proves that the effects of heat exchange in the energy loss and efficiency loss between piston and cylinder are critical. Finally, some suggestions are given for a better design of the axial piston pump.

1. Introduction

The axial piston pump (APP) is a positive displacement pump in a transmission system for high efficiency, power density, and structure compactness. Its popularity stems from its ability to control the effective fluid displacement per shaft revolution. Thanks to these capabilities and performance compared to other types of pumps, its demand and field of application have steadily increased in line with the time. This high demand in many applications leaded APP to face the problem of performance and efficiency losses. The piston/cylinder interface is one of the critical friction pairs presented in Fig. 1, which plays an essential role in the APP's lubrication mechanism and durability conditions.

The lubrication mechanism based on the behaviour of the physical properties of the solid-fluid structure is undoubtedly the appropriate medium to study and improve the performance of the APP. Developments in technology in the hydraulic fields recently imposed the need to build APPs that are increasingly sophisticated and capable of operating at very high speeds and pressures [1,2]. These new challenges also require innovative methods for preventing APP performance loss, and thermos-elastohydrodynamic deformation (TEHD) is unequivocally one of the appropriate methods to better predict the physical phenomena of the solid-fluid lubrication structure.

The energy loss and performance of APP on the piston-cylinder interface are mainly due to friction forces, leakage flow effects and deformation of the solid-liquid structure. Many types of research have been carried out on various aspects to address these problems. The fluid lubrication and structure improvement of APPs were conducted, considering various impact factors such as operating conditions, geometric parameters, materials' impact [3–9], texture and surface coating [10]. These researches on mixed solid-fluid structures and piston surfaces contribute to understanding the elastic deformation mechanism of piston and cylinder.

Some researchers have carried out works on heat exchange and the elastic deformation of the piston and the cylinder. Shang and Ivantysynova [11] have evaluated the temperature distribution in the piston as a function of piston size. Their study considered the heat transfer and generation in the liquid-solid structure and the solid body deformation due to pressure and thermal loading. Zhao et al. [12] have considered and studied a similar model. Pelosi and Ivantysynova [13] used the relief inertia method to calculate the elastic deformation affecting the stress mechanics on the piston and cylinder. Temperature distribution and elastic deformation were evaluated separately under specific operating conditions. Their calculation results showed that the elastic deformation of the piston and cylinder could be 2.84 μm and 5.5 μm, respectively, but the impact of temperature on the deformation was not taken into

* Corresponding author at: Zhejiang Normal University, Jinhua, Zhejiang 321004, China.
E-mail address: zsdwdy@zjnu.edu.cn (D. Wang).

https://doi.org/10.1016/j.triboint.2022.107846
Received 1 May 2022; Received in revised form 20 July 2022; Accepted 1 August 2022
Available online 3 August 2022

Nomenclature

B	Strain displacement matrix [-].
C	Constitutive matrix [-].
C_p	Heat capacity [$J.Kg^{-1}.K^{-1}$].
F_{fK}	Fluid force [N].
$F_{T,ax}$	Axial friction force [N].
$F_{T,tan}$	Tangential friction force [N].
F_{SK}	Swashplate reaction force [N].
F_{TB}	Slipper friction force [N].
F_{TK}	Piston friction force [N].
h	Fluid film thickness [μm].
k	The thermal conductivity [$W.\ \ m^{-1}.K^{-1}$].
p	Pressure [Pa].
Rb	Cylinder radius [m].
Rk	Piston radius [m].
t	Time [s].
T	The temperature [K].
q_v	The heat-flux density [W. m^{-2}].
u, v	Velocity components [$m.s^{-1}$].
β	Swashplate inclination angle [rad].
β_T	Volume expansion coefficient [$°C^{-1}$].
β_P	Compressibility coefficient [$m^{2/n}$].
τ	Shear stress [N/m^{-2}].
ϕ	Shaft speed [rad].
Φ_D	The mechanical dissipation term [W/m^3].
ρ	Liquid density [Kg/m^3].
ρ_0	initial liquid density [Kg/m^3].
σ	Viscous shear [Pa].
η	Fluid viscosity [Pa.s].
ω	Pump speed rotation [rad/s].
Π	Total potential energy [J].

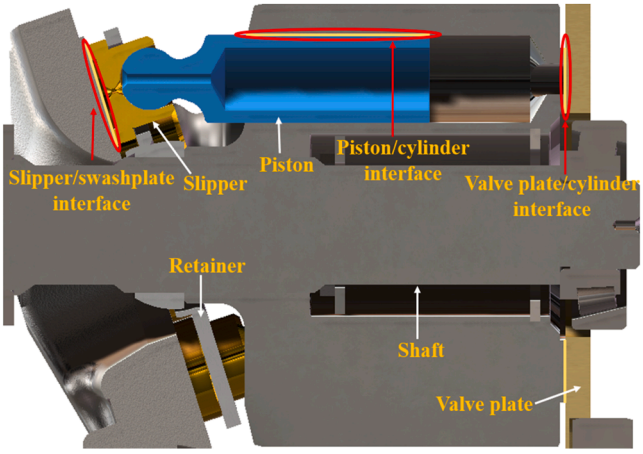

Fig. 1. The main lubricating interfaces in axial piston pumps.

account.

The use of TEHD would not only allow the practical evaluation of the heat exchange effects on the deformation of solid bodies but would also help to analyse the behaviour of the oil film thickness and between the piston and the cylinder. It is necessary to ensure good lubrication and predict the characterisation of the pressure of the corresponding film. The fluid pressure behaviour also makes it possible to analyse the carrying capacity of the piston to avoid possible solid-solid contact. Well-known researchers widely use the Reynolds equation to predict the film pressure [7,14,15] for calculating fluid pressure. Pelosi and Ivantysinova [16] conducted the pressure measurements and compared them with numerical results. The results enabled them to predict the behaviour of the film while considering the deformation of the piston and cylinder surface. Song et al. [17] conducted a numerical study of the influence of temperature on lubricating characteristics at the piston/cylinder interface based on flow speed's direction. However, the impact of elastic deformation was neglected. Nie et al. [18] researched the fluid structure between the piston and cylinder by evaluating the effect of elastic deformation on the oil thickness and the pressure. However, they did not consider the heat exchange effect in their work, which would significantly impact the analyses.

As one of the most significant sources of power loss between the piston and cylinder, viscous friction forces have attracted much attention in recent decades [19–21]. Manring [22] established a system for piston-cylinder friction based on lubrication conditions and a test device for measuring frictional characteristics in low-pressure and low-speed operations. Ma et al. [23] investigated the friction behaviour with the influences of the cylinder length, the clearance, and other structural parameters on the pump film thickness and the misalignment angle. Still, the effect of temperature on the lubricant was neglected. The temperature rise in the solid-liquid structure decreases the lubricant's viscosity and increases the leakage flow. Some researchers have done substantial work analysing and calculating the flow between the piston and cylinder. Bergada et al. [24,25] used analytic equations to develop full computational fluid dynamics (CFD) models to predict leakage flow between piston and cylinder block. Qian et al. [26] presented coupled thermal fluid-structure interaction model for the piston/cylinder interface leakage of a high-pressure fuel pump for diesel engines. They found that the thermal expansion of the cylinder is one of the most critical factors in increasing the leakage. The friction power loss and the structure interaction model were analysed [8] for the grooved piston/cylinder interface of various temperatures and piston/cylinder interface lengths [12]. The length varies with the piston motion, and their result demonstrated that the friction power loss increases slightly when the length increase from 0.25 to 1.

As previously stated, many researchers have studied the lubrication performances of piston/cylinder interface in axial piston pumps under isothermal conditions, and there is a significant number of investigations on the subject. However, few of these studies have used analytical methods to examine the interaction relationship between the elastohydrodynamic behaviour, the temperature effect and solid body deformation. The deformation of fluid and solid bodies considering the impact of temperature on the piston/cylinder interface is not studied.

This paper investigates the TEHD lubrication performance of the piston/cylinder interface. Under various operating conditions, pressure distribution, film thickness distribution, temperature, leakage, and friction losses are well discussed in the film gap between the piston and cylinder. The thermos-hydrodynamic deformation (THD) and TEHD models are compared for the lubricant properties, and the thermal effects on the lubrication mechanism and efficiency loss are investigated.

2. Mathematical modelling

It is known that energy loss is determined by the film properties, which depend on the eccentricity of the piston and the interface deformation (induced by pressure and thermal). Consequently, developing the TEHD method for the film is more than necessary to establish better concepts and predictions of the energy loss.

2.1. Film thickness

Considering the kinematic of the piston/cylinder assembly, the oil film between the piston and the cylinder can be expressed as follows [14]:

$$h(z_K,\varphi_K) = \sqrt{(R_b.cos\varphi_K - x(z_K))^2 + ((R_b.sin\varphi_K - y(z_K)))^2} - R_K(z_K) \quad (1)$$

where $h(z_K,\varphi_K)$ represents the oil film thickness at any position (z_K,φ_K). For any cross-section between 'A' and 'B' planes, the eccentric piston state is described in Fig. 2. Fig. 2(a) and (b) are respectively representing the inclined and top view of the 3D piston cylinder, while Fig. 2(c) represents a 2D cutting plan. (x_p, y_p, z_p) represents the centre positions of the piston; $(e_1,\ e_2)$ and $(e_3,\ e_4)$ represent respectively the eccentricity values at the 'A' and 'B' planes; R_k, R_b, φ_k represent respectively the piston radius, the cylinder radius, and the shaft angle.

$$\left\{\begin{matrix} x_P(z) = \dfrac{(e_3 - e_1)}{L}Z_P + e_1 \\ y_P(z) = \dfrac{(e_4 - e_2)}{L}Z_P + e_1 \end{matrix}\right\} \quad (2)$$

Eq. (2) represents the piston eccentricity equation. The initial eccentricity changing rate (e_1, e_2, e_3, e_4) is set to be (−0.00002, 0.00028, 0.00028, −0.000025), where they can be obtained using the Newton-Raphson method based on the eccentric motion equation of the piston, as follows:

$$(t+\Delta t), \quad \dot{e}_2(t+\Delta t), \quad \dot{e}_3(t+\Delta t), \quad \dot{e}_4(t+\Delta t) \quad (3)$$

Then the eccentricity acceleration $(\ddot{e}_1, \ddot{e}_2, \ddot{e}_3, \ddot{e}_4)$ at any time step is calculated with

$$\ddot{e}_i^k = \frac{\dot{e}_i(t+\Delta t) - \dot{e}_i(t)}{\Delta t}, \quad i = 1, \quad \ldots, \quad 4 \quad (4)$$

where "i" is the iteration number and Δt is the time difference, the convergence of the result is checked according to the following criterion:

$$\left|\frac{\ddot{e}_i^{k+1} - \ddot{e}_i^k}{\ddot{e}_i^{k+1}}\right| \le 10^{-7}, \quad i = 1,\ldots,4 \quad (5)$$

If Eq. (5) is satisfied, the next step will be carried out otherwise $[\dot{e}_1, \dot{e}_2, \dot{e}_3, \dot{e}_4]$ will be renewed.

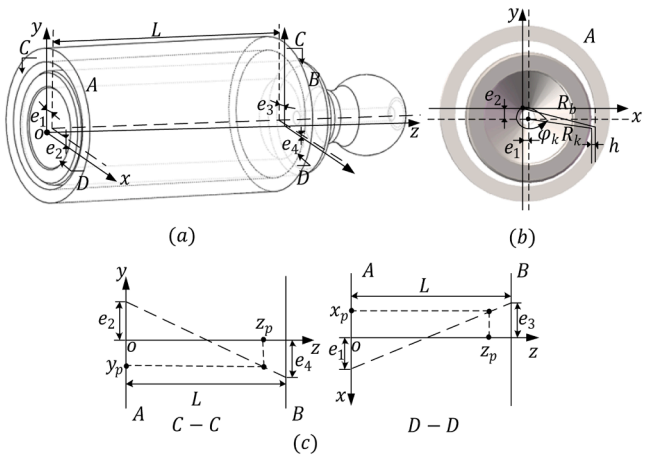

Fig. 2. Piston/cylinder chamber inclined section and definition of piston position.

2.2. Pressure distribution

To predict the fluid pressure, the well-known Reynolds equation has been derived by substituting the expression of the fluid velocities in the incompressible continuity equation and integrating it over the liquid film thickness direction [27,28]. Its cartesian coordinates' form is written as follows:

$$\frac{\partial}{\partial\hat{x}}\left(h^3\frac{\partial p}{\partial\hat{x}}\right) + \frac{\partial}{\partial\hat{y}}\left(h^3\frac{\partial p}{\partial\hat{y}}\right) + 6\mu\left[\begin{matrix} \hat{u}_k\left(2\dfrac{\partial|h_b|}{\partial\hat{x}} - \dfrac{\partial h}{\partial\hat{x}}\right) \\ +\hat{v}_k\left(2\dfrac{\partial|h_b|}{\partial\hat{y}} - \dfrac{\partial h}{\partial\hat{y}}\right) + 2\dfrac{\partial h}{\partial t}\end{matrix}\right] = 0 \quad (6)$$

In Eq. (1), the film thickness $h(x,y,t)$, the shear velocities $u(x,y,t)$ and $v(x,y,t)$ will be given by the previous time step. By solving numerically Eq. (6), the pressure $p(x,y,t)$ can be obtained and then used to derive the flow velocities and the stresses. $\hat{u}$ and $\hat{v}$ are equal to 0 when $z = 0$ and respectively equal to constant values u_k and v_k when $z = h$.

2.3. Friction force

Between the piston and the cylinder block, the viscous friction forces change dynamically during the revolution of the shaft due to the APP kinematics and oscillating load conditions. Therefore, the rotational speed and the shaft angle φ significantly influence its behaviour.

The loads exerted on the piston body are represented in Fig. 3, where P_D is a displacement chamber pressure, F_{DK} is the displacement pressure force, the viscous friction force F_{TK}, axial force F_{AKz}, transversal force F_{Sky}, swashplate reaction force F_{SK}, centrifugal force $F_{\omega K}$, and the viscous friction force between a piston and cylinder F_{TG}. Fig. 4.

Using the boundary of the given condition in 2.2, the flow velocity can be given as follows:

$$\left\{\begin{matrix} \hat{u} = \dfrac{1}{2\mu}\dfrac{\partial p}{\partial\hat{x}}\left(\hat{z}^2 - h\hat{z}\right) + \dfrac{\hat{z}}{h}u_k \\ \hat{v} = \dfrac{1}{2\mu}\dfrac{\partial p}{\partial\hat{y}}\left(\hat{z}^2 - h\hat{z}\right) + \dfrac{\hat{z}}{h}v_k \end{matrix}\right\} \quad (7)$$

where $u_k = \omega.R_b$, $v_k = -\omega.R_b.\tan\beta.\sin\varphi$, $\frac{\partial p}{\partial\hat{x}}$ and $\frac{\partial p}{\partial\hat{y}}$ can be obtained by solving Eq. (6). From the fluid velocity distribution given in Eq. (7), the shear stresses on the piston and cylinder surface are determinable considering the fluid flow as Newtonian flow. $\hat{x} = (d_K/2)\phi_K$, $\hat{y} = z_K$ and $\hat{z} = h$.

Using Eq. (7) the shear stresses acting on the piston surface equation can be calculated as follows:

$$\left\{\begin{matrix} \tau_{\hat{x}} = \mu.\dfrac{\partial v_{\hat{x}}}{\partial z} = \mu.\dfrac{u_K}{h} + \dfrac{\partial p}{\partial\hat{x}}\left(\hat{z} - \dfrac{h}{2}\right) \\ \tau_{\hat{y}} = \mu.\dfrac{\partial v_{\hat{y}}}{\partial z} = \mu.\dfrac{u_K}{h} + \dfrac{\partial p}{\partial\hat{y}}\left(\hat{z} - \dfrac{h}{2}\right) \end{matrix}\right\} \quad (8)$$

$$F_T(\varphi) = \int_A \tau(\varphi)dA \quad (9)$$

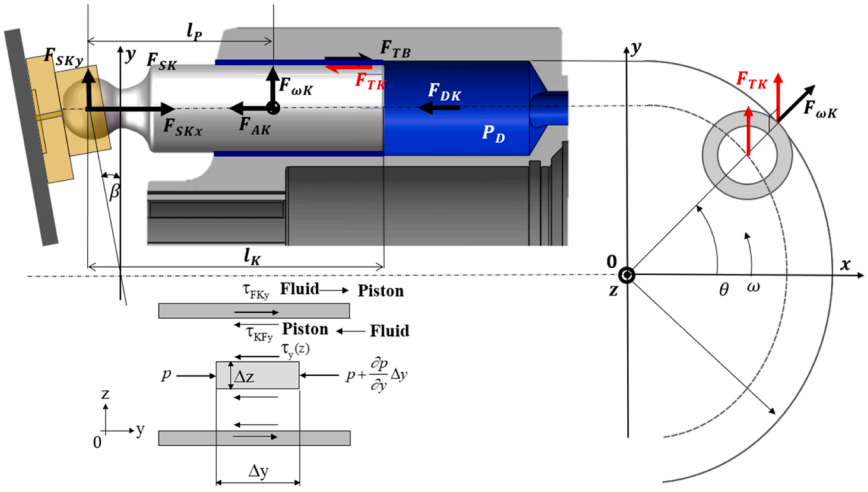

Fig. 3. Piston forces diagram.

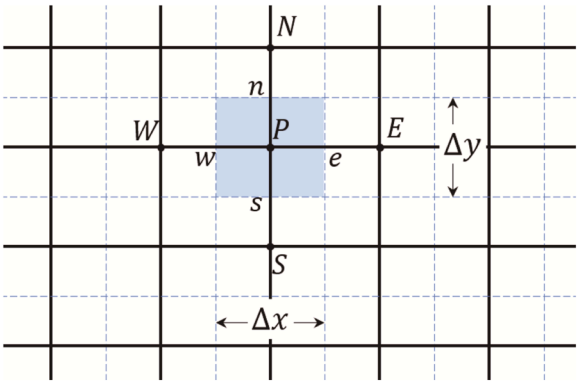

Fig. 4. 2D dimension grid discretisation.

$$\left\{\begin{array}{ll} F_{T,tan} = \int_0^{\pi D_K}\int_0^{\hat{y}_{max}} \tau_{\hat{x}} d\hat{y} d\hat{x} & (a) \\ F_{T,ax} = \int_0^{\pi D_K}\int_0^{\hat{y}_{max}} \tau_{\hat{y}} d\hat{y} d\hat{x} & (b) \end{array}\right\} \tag{10}$$

Eq. (9) gives the general expression of the viscous friction force acting on the piston, which can be broken down into two components, the tangential and axial components, as given in Eq. (10) (a) and (b).

2.4. Leakage flow model

The volumetric loss, one of the direct power losses on the piston/cylinder interface, is derived from the velocity distribution integration in Eq. (7). Due to the different conditions encountered by the piston/cylinder interface, the leakage flow varies during one shaft revolution, namely a function of shaft angle [27]. The expression of the instantaneous leakage flow for one single piston $Q_{CP1}(\varphi)$ and leakage flow for pistons $Q_{CP}(\varphi)$ can be obtained by Eq. (11); where Z is the piston number and 'a' is the angular separation of piston and it is equal to 360°/Z.

$$\left\{\begin{array}{l} Q_{CP1}(\varphi) = \int_0^{2\pi} \left(\frac{h^3}{3\mu}\frac{\partial p}{\partial z} - \frac{v_s h}{2}\right) R d\theta \\ Q_{CP}(\varphi) = \sum_{i=0}^{(Z+1)/2-1} Q_{CP1}(\varphi + ia) \end{array}\right\} \tag{11}$$

2.5. Energy equation

The thermal model is a critical part of the lubrication mechanism APP since the heat deforms the interfaces and decreases the lubricant viscosity. The energy equation in Eq. (12) is considered in the non-isothermal fluid flow numerical model for predicting the temperature distribution in the fluid film within the gap. According to [3], the time derivative of temperature is negligible; thus, the energy equation we applied is in the form:

$$c_P\left(v_{\hat{x}}\frac{\partial T}{\partial \hat{x}} + v_{\hat{y}}\frac{\partial T}{\partial \hat{y}}\right) = \frac{1}{\rho}\left[\begin{array}{c} \frac{\partial}{\partial \hat{x}}\left(\lambda\frac{\partial T}{\partial \hat{x}}\right) + \frac{\partial}{\partial \hat{y}}\left(\lambda\frac{\partial T}{\partial \hat{y}}\right) \\ + \frac{\partial y}{\partial \hat{z}}\left(\lambda\frac{\partial T}{\partial \hat{z}}\right) \end{array}\right] + \frac{\mu}{\rho}\Phi_D \tag{12}$$

where Φ_D represents the mechanical dissipation term

$$\Phi_D = \left(\frac{\partial \hat{u}}{\partial \hat{z}}\right)^2 + \left(\frac{\partial \hat{v}}{\partial \hat{z}}\right)^2 \tag{13}$$

According to [29], the liquid viscosity can be expressed as a function of the temperature

$$\mu = \mu_0 . exp\left(\alpha_p p - k_T (T - T_0)\right) \tag{14}$$

where μ_0 is the reference fluid viscosity; α_p is the viscosity pressure coefficient; k_T is the viscous temperature coefficient.

2.6. Solid heat transfer and deformation

To calculate the elastic deformation of the solid bodies (piston and cylinder), the fundamental finite element analysis of the potential energy dissipation equation and methodology proposed by Schenk and Ivantysynova [30] consists of analysing numerically one single part and extending. The total potential energy in the element expressed in Eq. (15) element nodal forces are derived from external pressure loads and internal thermal stress,

$$\Pi = U_\varepsilon + V_{NF} = \frac{1}{2}\int_V (Bu)^T C(Bu)dV - u^T \begin{Bmatrix} F_{x1} \\ F_{y1} \\ F_{z1} \\ \vdots \\ F_{xn} \\ F_{yn} \\ F_{zn} \end{Bmatrix} \tag{15}$$

where β_T, β_P and ρ_0 represent the volume expansion coefficient, the compressibility coefficient and the initial oil density, respectively; U_ε the nodal forces vector due to thermal-induced stress and V_{NF} the nodal forces vector due to external loads.

2.7. Power loss

The total power loss between piston and cylinder block in APP is the combination of the loss due to the viscous friction force (P_{ST}) and the loss due to the leakage (P_{SQ}), which can be expressed in the following equations:

$$P_{ST} = \mu \frac{v^2}{h} b.l. \tag{16}$$

$$P_{SQ} = \frac{1}{12\mu}\frac{\Delta p^2}{l} b.h^3 \tag{17}$$

where b represents the width of the sealing land , l is the piston length. Thus, the expression of the total power loss between piston and cylinder block is given as follows:

$$P_S = P_{ST} + P_{SQ} \tag{18}$$

3. Calculation and simulation

3.1. Numerical methods

Based on the mathematical modelling described in the previous part, the numerical solution of the lubricant parameters, including its film thickness, pressure and temperature model, is described below.

Eq. (1) is used for calculating the oil film thickness, which will be incremented into the Reynolds equation, Eq. (6), to calculate fluid film pressure using the finite volume method.

$$\begin{Bmatrix} p_{i-1,j} = p_{i,j} - \Delta x_p \left|\frac{\partial p}{\partial x_p}\right|_{i,j} + \frac{1}{2}\Delta {x_p}^2 \left|\frac{\partial^2 p}{\partial {x_p}^2}\right|_{i,j} - \cdots \\ p_{i+1,j} = p_{i,j} + \Delta x_p \left|\frac{\partial p}{\partial x_p}\right|_{i,j} + \frac{1}{2}\Delta {x_p}^2 \left|\frac{\partial^2 p}{\partial {x_p}^2}\right|_{i,j} + \cdots \\ p_{i,j-1} = p_{i,j} - \Delta y_p \left|\frac{\partial p}{\partial y_p}\right|_{i,j} + \frac{1}{2}\Delta {y_p}^2 \left|\frac{\partial^2 p}{\partial {y_p}^2}\right|_{i,j} - \cdots \\ p_{i,j+1} = p_{i,j} + \Delta y_p \left|\frac{\partial p}{\partial y_p}\right|_{i,j} + \frac{1}{2}\Delta {y_p}^2 \left|\frac{\partial^2 p}{\partial {y_p}^2}\right|_{i,j} + \cdots \end{Bmatrix} \tag{19}$$

By neglecting the higher-order terms of Eq. (19), its approximation can allow us to quickly find the terms of the partial derivatives of the pressure field as follows:

$$\begin{Bmatrix} \frac{\partial p_{ij}}{\partial x} = \frac{p_{i+1,j} - p_{i-1,j}}{2\Delta x} & (a) \\ \frac{\partial p_{ij}}{\partial y} = \frac{p_{i,j+1} - p_{i,j-1}}{2\Delta x} & (b) \end{Bmatrix} \tag{20}$$

$$\begin{Bmatrix} \frac{\partial^2 p}{\partial x^2} = \frac{p_{i+1,j} - 2p_{i,j} + p_{i-1,j}}{\Delta x^2} & (a) \\ \frac{\partial^2 p}{\partial y^2} = \frac{p_{i,j+1} - 2p_{i,j} + p_{i,j-1}}{\Delta y^2} & (b) \end{Bmatrix} \tag{21}$$

Substituting Eqs. (19), (20) and (21) into Eq. (6), we can obtain:

$$p_{i,j}^{(k+1)} = \frac{\left(1 + \frac{3}{2}\Delta x_p \frac{\partial h}{\partial x}\right)}{2 + 2\left(\frac{\Delta x_p}{\Delta y_p}\right)^2} p_{i+1,j}^{(k)} + \frac{\left(1 + \frac{3}{2}\Delta y_p \frac{\partial h}{\partial z}\right)}{2 + 2\left(\frac{\Delta y_p}{\Delta x_p}\right)^2} p_{i,j+1}^{(k)} + \frac{\left(1 - \frac{3}{2}\Delta x_p \frac{\partial h}{\partial x}\right)}{2 + 2\left(\frac{\Delta x}{\Delta y_p}\right)^2} p_{i-1,j}^{(k+1)} + \frac{\left(1 - \frac{3}{2}\Delta y_p \frac{\partial h}{\partial z}\right)}{2 + 2\left(\frac{\Delta y_p}{\Delta x_p}\right)^2} p_{i,j-1}^{(k+1)} - \frac{6\left(u_k \frac{\partial h}{\partial x_p} + v_k \frac{\partial h}{\partial y_p}\right)}{\left(\frac{2h^3}{\mu(\Delta x_p)^2} + \frac{2h^3}{\mu(\Delta y_p)^2}\right)} \tag{22}$$

By setting A_{ij}, B_{ij}, C_{ij}, D_{ij} and E_{ij} in Eq. (22) equal to these following values, respectively,

$A_{ij} = \frac{\left(1+\frac{3}{2}\Delta x_p \frac{\partial h}{\partial x}\right)}{2+2\left(\frac{\Delta x_p}{\Delta y_p}\right)^2}$, $B_{ij} = \frac{\left(1+\frac{3}{2}\Delta y_p \frac{\partial h}{\partial z}\right)}{2+2\left(\frac{\Delta y_p}{\Delta x_p}\right)^2}$, $C_{ij} = \frac{\left(1-\frac{3}{2}\Delta x_p \frac{\partial h}{\partial x}\right)}{2+2\left(\frac{\Delta x}{\Delta y_p}\right)^2}$, $D_{ij} = \frac{\left(1-\frac{3}{2}\Delta y_p \frac{\partial h}{\partial z}\right)}{2+2\left(\frac{\Delta y_p}{\Delta x_p}\right)^2}$ and $E_{ij} = -\frac{6\left(u_k \frac{\partial h}{\partial x_p} + v_k \frac{\partial h}{\partial y_p}\right)}{\left(\frac{2h^3}{\mu(\Delta x_p)^2} + \frac{2h^3}{\mu(\Delta y_p)^2}\right)}$

the pressure at any single point P_{ij} can be written as follows:

$$\begin{aligned} p_{i,j} = {} & A_{i,j}.p_{i+1,j} + B_{i,j}.p_{i-1,j} + \\ & C_{i,j}.p_{i,j+1} + D_{i,j}.p_{i,j-1} + E_{i,j} \end{aligned} \tag{23}$$

Knowing the lubricant's characteristics can help determine its capacity to resist the maximum heat, maintain a suitable lubrication mechanism and prevent wear from friction and eventual solid body contact. It is critical to emphasise that the contact of solid bodies is the direct cause of the exaggerated deformation, damage, or cracks of the piston and cylinder block in the APP.

The temperature is obtainable by the resolution of Eq. (12) energy equation), using the similar method as described and used to calculate the pressure above. The balance for the generation of the heat diffusion, Eq. (13) in the control volume, the fluxes through the piston cell surface are determined. The linear tetrahedral elements can be used to discretise the solid body for the thermal conductive analysis.

Fig. 5(a) presents the solid body meshing type, and Fig. 5(b) gives the piston surface open domain and its Finite Volume Domain discretisation. The solution of the diffusive form of the energy equation is obtained for mechanical body parts. The temperature distribution is used to determine the thermal stress condition for the solid parts and as a more accurate surface temperature boundary, T, for the fluid film. For the piston and cylinder mechanical bodies, the solution of the linear system of elastic equations is obtained. The elastic deformation of the solids is determined using external pressure and internal temperature loads. An iterative method is used to obtain the solution of pressure surface elastic deformation while running the complete FEM analysis offline. The thermal deformation is solved by running the entire FEM analysis.

Thus, the same Cartesian to natural coordinate transformations apply. Like the elastic linear tetrahedron, the temperature field is assumed to be a weighted linear combination of the four nodal temperatures, as shown in Fig. 5(a). The temperature of a point with natural

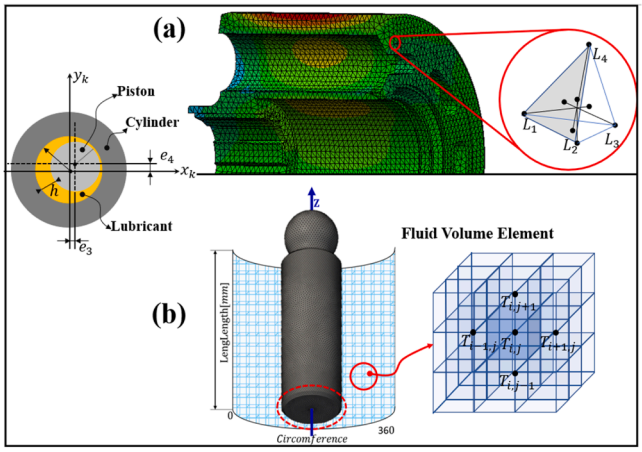

Fig. 5. Calculation domain and meshing types for solid (a) and fluid (b).

coordinates ($L1$, $L2$, $L3$, $L4$) is interpolated where.

$T_P = [T_1 \quad T_2 \quad T_3\, T_4]\{L_1 \quad L_2 \quad L_3 \quad L_4 \quad\}^T$ and $T(x,y,z) = [N_1 \quad N_2 \quad N_3\, N_4]\{L_1 \quad L_2 \quad L_3 \quad L_4 \quad\}^T$. One of the necessary conditions to avoid contact between solid bodies is to ensure that the set of external forces applied to the piston should not be greater than the fluid pressure force in the cylinder chamber.

Fig. 6 presents the complete solution scheme of the simulation model. The parameters are solved at discrete intervals corresponding to a progressive increasing shaft rotation and different load conditions. The Reynolds and the energy equations, respectively, given by Eq. (6) and Eq. (13) are solved on a finite volume discretised domain. The most inner loop helps in solving the non-isothermal fluid film flow equations. The fluid properties, including viscosity, density and the surface elastic deformation due to the dynamic pressure field, are updated at each iteration. The rigid constraint condition determines the pressure and thermal elastic deformations.

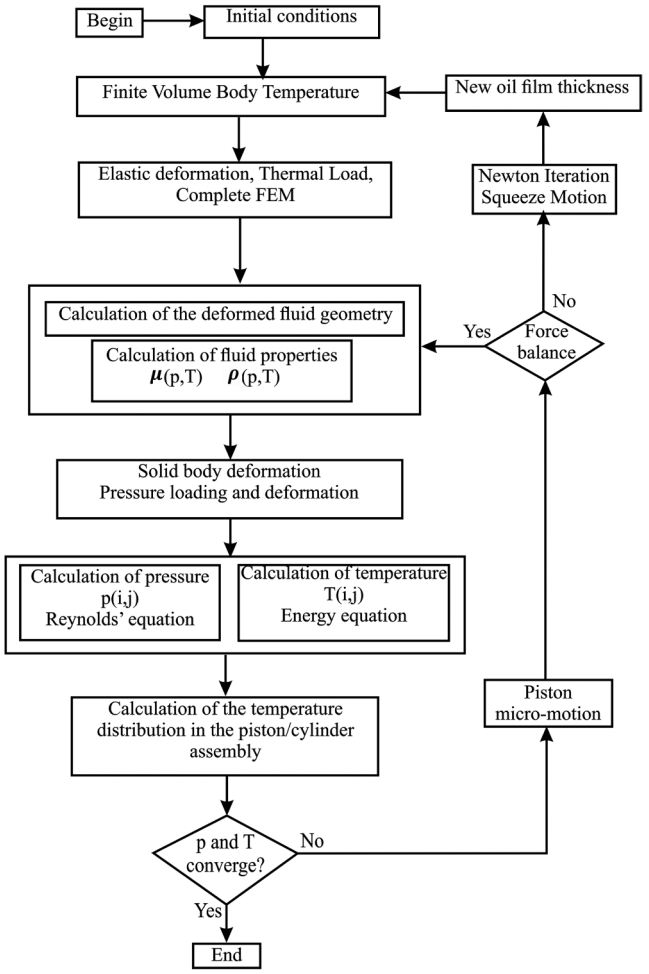

Fig. 6. The complete fully-coupled solution flow chart.

The solid-body deformation and temperature are calculated using the tetrahedron finite mesh element analysis. Here, the analysis is approached as a partitioned fluid-structure interaction analysis, with the nonlinearity accounted for by an iterative Picard scheme on the outside [31]. As a result, pressure-deformation convergence is achieved by employing a smart under-relaxed fixed point Picard iteration that adjusts the under-relaxation coefficients proportionally to the pressure residual behaviour. The thermo-elastohydrodynamic fluid film described thus far represents the algorithm's core, where the most inner loop solves the non-isothermal fluid film flow equations iteratively. The fluid properties and surface elastic deformation caused by the dynamic pressure field are updated at each iteration step. The fluid film geometry determines the fluid film pressure build-up, which continuously changes over one shaft revolution due to the piston's oscillating external loads and relative motion to balance the changing external loads. The hydrodynamic pressure that builds up in the fluid film must generate enough fluid forces and moments to balance the external ones defined in part 2.3.

3.2. Solids and fluid properties

This part contains information on the properties of the solids (piston and cylinder) and the lubricant used for numerical calculations and simulations. The table arranges this information as follows: Table 1 shows the dimensions of the piston and cylinder; Table 2 contains the mechanical properties of the piston and the cylinder; and finally, Table 3 shows the properties and characteristics of the viscous liquid used as a lubricant.

4. Results and discussions

4.1. Validation of the results

The oil temperature is chosen and compared with other published works to validate our model. We used similar operating parameters and boundary conditions to simulate the temperature distribution and compared it with the experiment performed by Pelosi and Ivantysynova [16]. The initial conditions and input values are as follows: the differential pressure of 22.5 MPa, shaft rotational speed of 1000 RPM, and the temperature of high and low-pressure ports are respectively 48 ℃ and 43 ℃. Fig. 7(a) presents a simulated piston/cylinder interface, and Fig. 7 (b) depicts the measurement result carried out in [16]. These results show that the model could describe the oil temperature behaviour and distribution well.

Table 1
Piston and cylinder dimensions.

Dimensions	Values [mm]
Piston Inner diameter	12
Piston outer diameter	17
Diameter of the piston's head hole	2
Piston length	45
Cylinder hole's diameter	17.012
Length of the cylinder hole	57

Table 2
Mechanical properties of piston and cylinder block.

	Piston	Cylinder
Mechanical Properties	20CrMnTi Steel	ZQAl9–4 Steel
Yield [MPa]	415	923
Tensile [MPa]	520	333
Shear modulus [MPa]	80000	81000
Poisson's ratio	0.28	0.30
Thermal conductivity [W/m.K]	46.60	42.20
Mass density [Kg/m^3]	7800	7900
Elasticity [N/mm^2]	207 GPa	117 GPa

Table 3
Fluid properties.

Parameters [units]	Values
Dynamic oil viscosity [Pa.s]	0.070
Oil density [kg/m^3]	1035
Heat conductivity of oil [W/m.K]	0.037
Heat capacity oil [J/kg.K]	2000
Kinematic viscosity pressure coefficient [–]	1.5e^{-13}
Thermal conductivity of oil [W/m.K]	0.037
Kinematic viscosity weighting factor [–]	0.900
Kinematic viscosity-temperature coef. [–]	3.787

4.2. General results

During the normal working condition of APP, the first half rotation angle (between 0° and 180°) is subjected to high displacement chamber pressure and the second half (from 180° to 360°) is at low pressure. The piston displacement path can also overflow the initial and statical path that the piston would follow when coaxial; the results of piston movement are shown in Fig. 8. The displacement diagram shows the movement of the piston axis within the piston clearance. On the displacement path, the piston position is marked for some angles of rotation of the cylinder block.

In the normal working condition of APP, during the compression (0–180°), the external loads on the piston become enormous due to the compressive forces. Therefore, the piston tilts strongly in the liner to compensate for these transverse forces. Subsequently, the displacement path is very close to the edge of the piston clearance, and minimal gap heights occur. However, in the suction zone (180–360°), only a low external force load occurs, and the displacement path is not so close to the edge of the piston clearance. As a result, the gap heights increase, and temperature decreases the lubricant viscosity, increasing viscous friction forces.

Fig. 9 shows the behaviour of the viscous fluid properties between the piston and cylindrical block. The simulation domain is the opened piston surface, as shown in Fig. 5(b). Each simulated parameter (p, $h$and$T$) is presented for four different chosen angles (45°, 90°, 180°, and315°). The numerical calculations are performed at a rotational speed of 3000 rpm, and the higher pressure is set at 40 MPa. Due to the critical role that the gap height plays in determining the pressure fields,

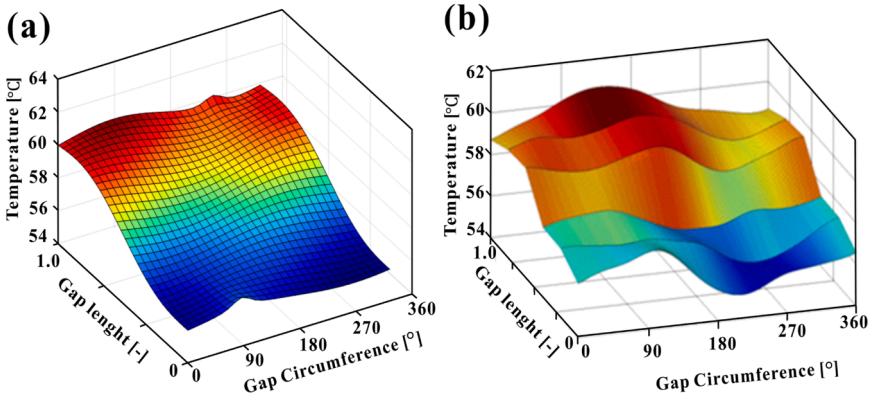

Fig. 7. (a) Our simulated temperature results; (b) Measurement results from [16].

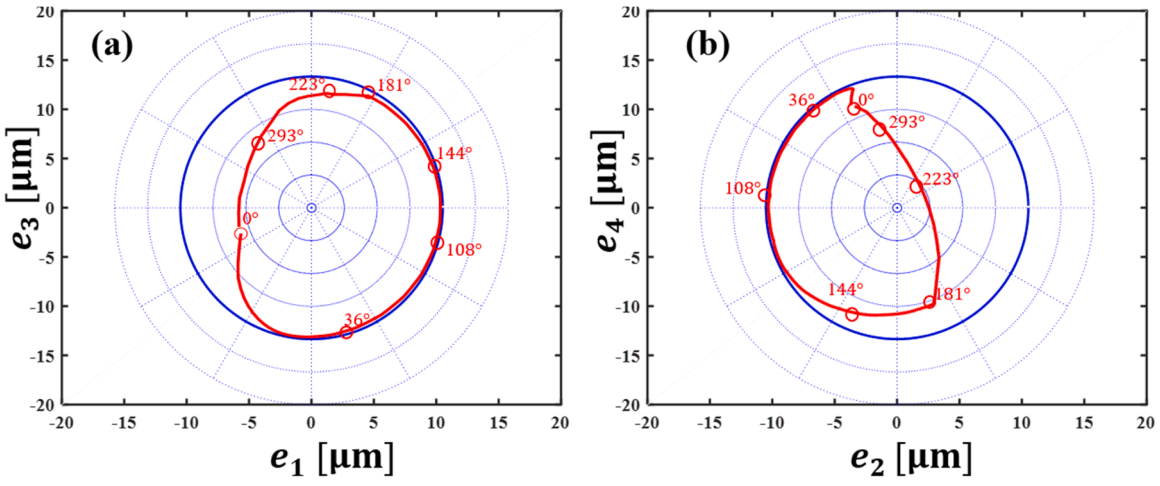

Fig. 8. Piston coordinates motions, e_3 sab e_1 (a) and e_4 sab $e_2(b)$.

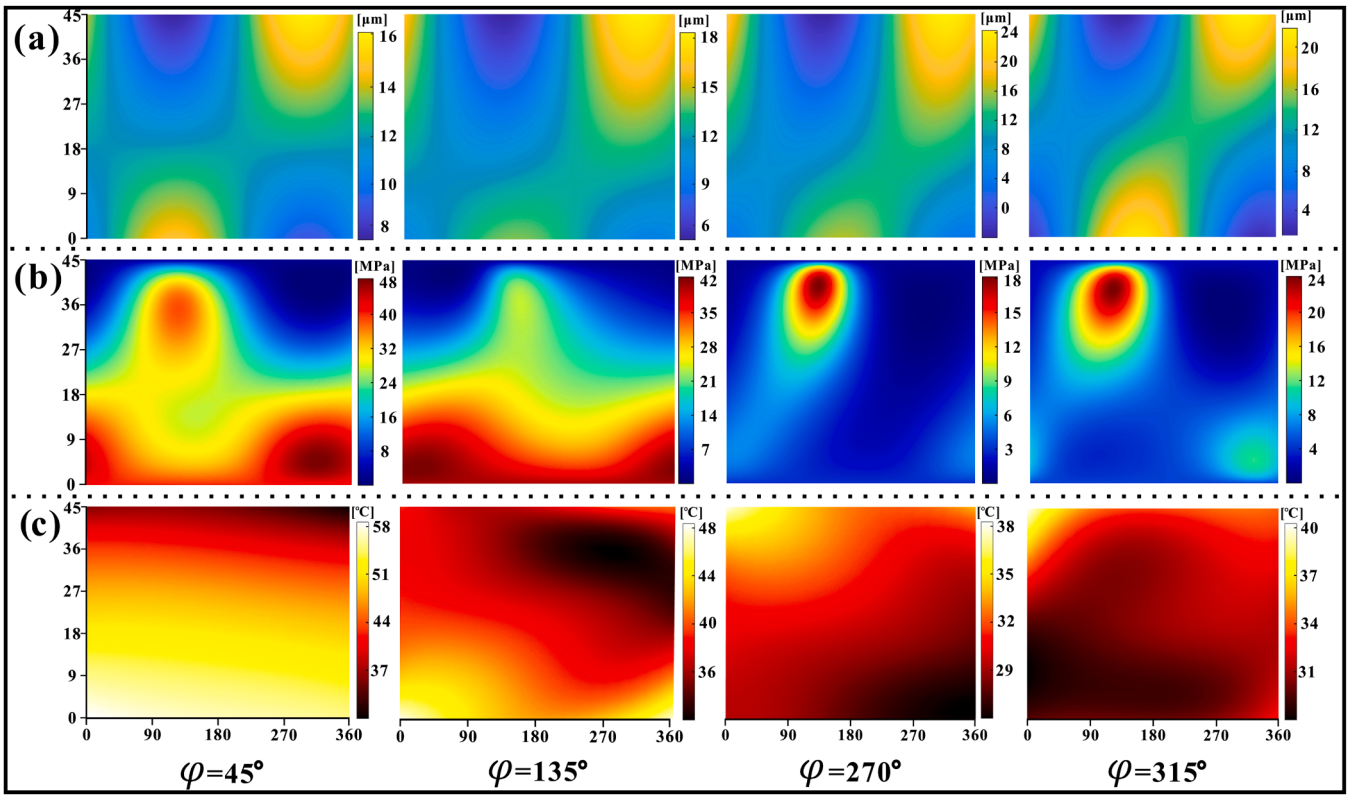

Fig. 9. (a) Fluid film thickness (1st row), (b) fluid film pressure (2nd row) and (c) temperature distribution (3rd row) on the piston/cylinder interface in APP over one shaft revolution.

it is first calculated using Eq. (1). As presented in Fig. 9, the first raw (a) gives the viscous oil film thickness, (b) gives the hydrodynamic oil film pressure and (c) the oil film temperature.

For one shaft revolution, the external load is higher between 0° and 180° (loading or pressurising zone). Therefore, the oil film pressure is also higher, and the oil film thickness becomes small (minimal). This proportional inverse relationship can be explained by the pressure gradient relying on the second derivatives of shearing velocities in the creeping flow. For a certain shaft rotation angle, the maximum difference of the pressure varies up to 24 MPa, while the maximum difference of the fluid film thickness varies up to 8 μm. We can also observe that higher pressure generally corresponds to a thinner film (vice versa), as reported in the literature [16]. Given certain shearing velocities (depending on the piston motion), a thinner film will lead to a larger pressure gradient, hence a higher pressure.

Furthermore, this proportional inverse relationship prevents the eccentricity from increasing consistently, i.e., helping to maintain the film. Our results also show similarities with the research results conducted by Nie et al. [18] regarding areas with high and low oil gaps. At the same time, the differences between the maximum fluid thickness for different angles are not as wide as theirs. As we can see in Fig. 9(a), the difference in oil thickness between 45° and 135° angle position is 2 μm, and between 270° and 315° is 3 μm. This is relatively small compared to their result, which is 12.2 μm for between 90° and 270°. Fig. 9(b) demonstrates the change in hydrodynamic pressure distribution at the piston/cylinder interface for 45°, 90°, 180°, and 315°. The difference in pressure between 135° and 270° angle positions is 18 MPa. Proceeding the same comparison same angle positions from [12], we get 14 MPa. This confirms the validity of the results of our model.

4.3. The impact of elastic and hydrodynamic deformation on the lubrication mechanism

The external pressure force acting in the displacement chamber leads the entire block to bend around the constrained splined surface. A three-dimensional solid body heat transfer model calculates the solid temperature profile. The piston and cylinder bodies' deformation is performed to show the real heat impact of the transfer on the deformation of the solid bodies. Fig. 10(a) shows the elastic deformation without the thermal effect, while Fig. 10(b) shows the thermoelastic deformation of the solid bodies. It is visible that the thermal effect is significantly enlarging the elastic deformation of both piston and cylinder block. We can see that the deformation increases by 8 μm for the cylinder and 2.2 μm for the piston.

The piston body deformation plays a significant role in the mechanism and lubrication process of the piston/cylinder interface, especially in terms of the maximum fluid thickness. The applied external pressure highly influences the deformation. Fig. 11 compares the oil film thickness and pressure film distribution calculated by THD (a) and TEHD (b). Due to the external load on the piston, the variation amplitude of film thickness decreases significantly with increasing load pressure. The maximum dynamic film thickness increases by 4 μm (4%) while the oil pressure increases by 5 MPa (20%) as the deformation is considered. It is explained by the fact that the elastic deformation of the solid body creates more gaps between the piston and cylinder.

Furthermore, the hydrodynamic pressure effect causes visible elastic deformation of the piston surface. Comparing our results with those of reference [32], which did not take into account the effects of temperature, we can note that the impact of elastic deformation increases the maximum oil thickness by more than 42% for the angular position of 90° and by more than 24% for 270°. This large increase in the fluid gap without the thermal effects seems more critical to an excellent lubrication mechanism.

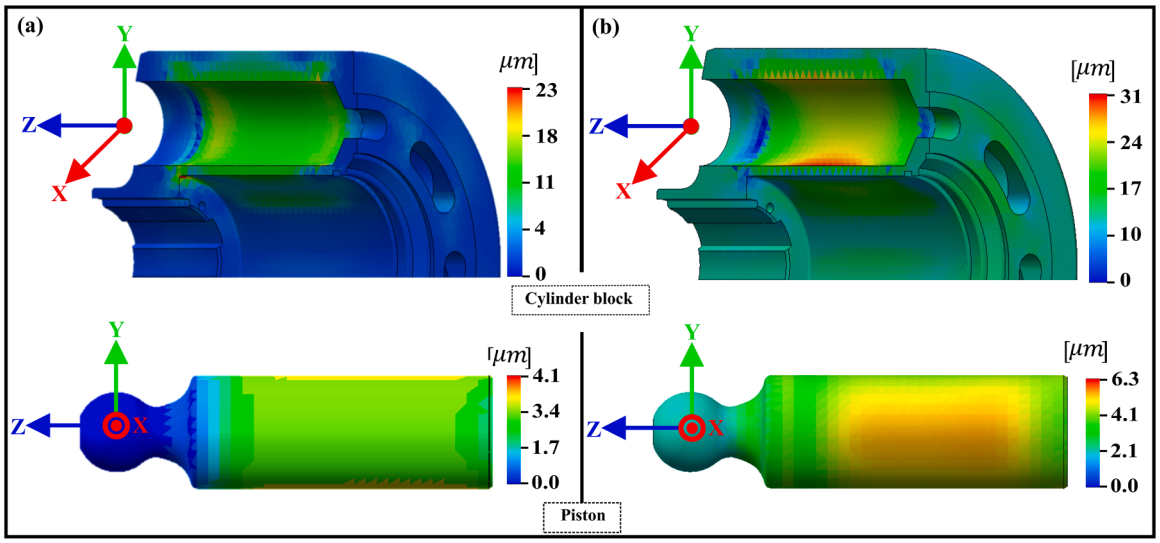

Fig. 10. Elastic deformation (a) and thermoelastic deformation (b) of the cylinder block and piston. The applied load is 12 MPa; the initial body temperature of the cylinder block is 41 ℃.

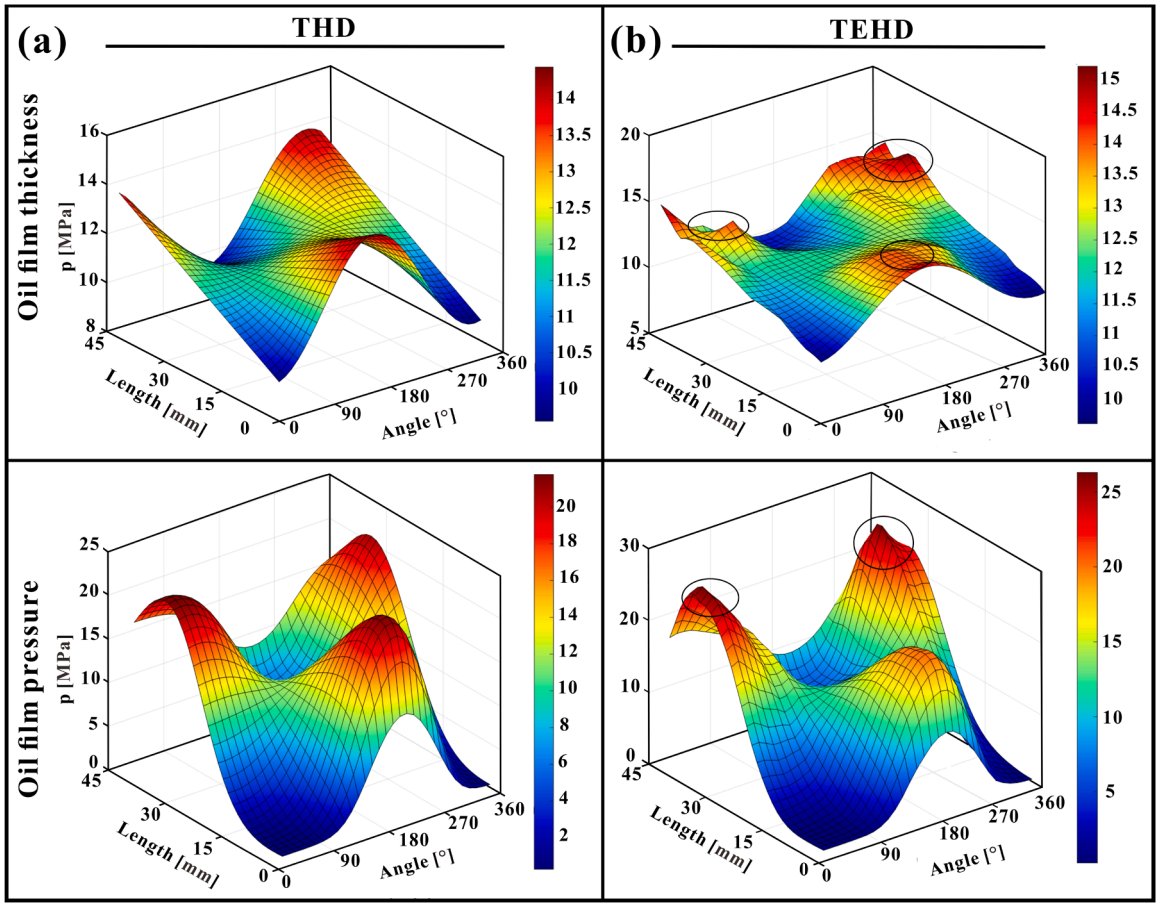

Fig. 11. Fluid film thickness and pressure between piston and cylinder block, (a) THD and (b) TEHD, for one shaft rotation.

4.4. Impact of the heat and operating parameters on the viscous friction force and leakage flow

To better understand the behaviour of the axial friction forces during the normal working condition of APP, several parameters are considered during the numerical computation using Eq. (10). Results are presented in Fig. 12 as follows: (a) for three different values of viscosity (100 ℃, 80 ℃ and 20 ℃) with a fixed shaft speed (1200 rpm); (b) for three different values of shaft speed (1000, 1500 and 2000 rpm) with a fixed load (30 MPa); (c) for three different values of loads (40, 20 and 5 MPa) with a fixed shaft speed (1200 rpm).

It is worth noting that axial friction forces appear to be proportional to the load. Similar results have been found by Ivantysynova and Lasaar [3], where a comparison of axial friction forces with the standard

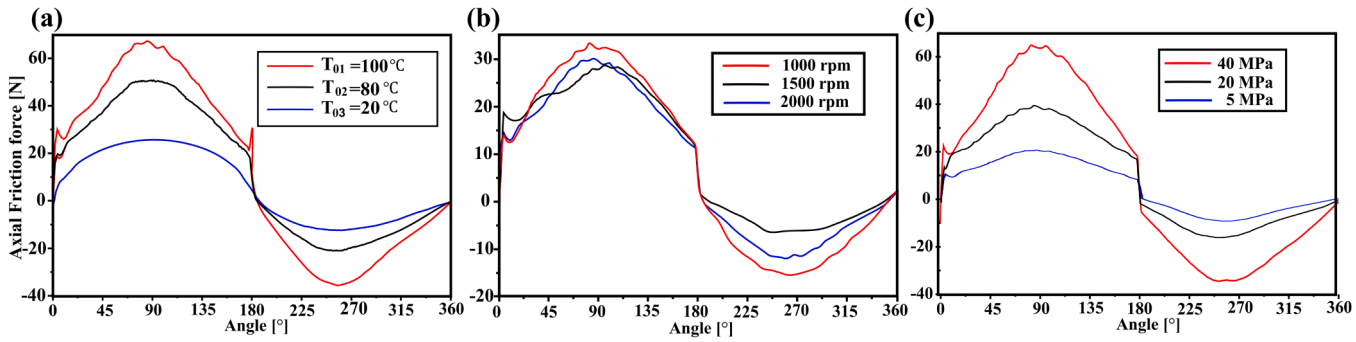

Fig. 12. Axial friction force: (a) for different values of temperature, (b) for different values of shaft speed, (c) for different values of the applied load.

CASPAR version and measurement assuming rigid and EHD part simulation. The simulation results of this work fit better with their measurements, especially for the high-pressure value.

It is also noticeable that the influence of viscosity on both axial and tangential friction forces is imminent. According to the simulation result in Fig. 12(a), the increase of initial oil temperature from 20 ℃ to 80 ℃ increases the maximum axial friction force from 20 N to 45 N. And if the initial oil temperature changes from 20 ℃ to 100 ℃, the maximum axial friction force increases by 44N. Similar remarks can be made for axial friction forces by varying the shaft rotational speed and applied load in Fig. 12(b) and (c). The behaviour of the axial friction forces for different shaft speeds is not as linear as for the applied loads. From Fig. 12(c), it can be concluded that axial friction forces are proportional to the applied load. This helps to analyse the piston load carrying capacity and the impact of external force on the power loss due to friction forces. The pressure difference and the piston movement affect the gap volume flow. There is almost no pressure difference with the suction stroke, and the gap volume flow is caused only by the piston movement. To give a view of the leakage flow behaviour in the normal working condition of APP, three parameters, which are initial oil temperature, piston clearance and external load have been chosen as variables. Three different values have been given to each variable for the numerical calculation, as we can see in Fig. 13.

The influence of the temperature (through the oil viscosity), the pressure (load) and the piston clearance on gap volume flow are clearly visible. As it can be observed, the gap volume flow has a minimum value at a rotation angle of $\varphi = 90^{\circ}$ at maximum axial piston speed. Although our model is unique in terms of length and dimensions, the results match the shapes of other published work results [32]. Fig. 13(a) gives the influence of temperature on the volume flow between piston and cylinder block. The decrease of 20 ℃ in temperature leads to the rise of leakage flow up to 0.032 L/min. Fig. 13(b) presents the impact of the piston clearance on the gap volume flow. With three different given values of the clearance, it is observable that the gap volume flow increases with increasing piston clearance. It is observable that the leakage flow increases and becomes less stable when to increase the clearance between piston and cylinder. Similarly, Fig. 13(c) shows how the leakage flow increase with the pressure (applied load). The leakage flow varies proportional variation of the leakage flow with pressure in the loading zone (0–180°) can reach the difference of about 0.07 L/min in a maximum value while it remains almost the same in the discharge zone (180–370°).

4.5. Friction power losses

Fig. 14 compares the friction power losses behaviours on the piston/cylinder interface for three different values of oil temperature, pressure and gap. As the load increases, the viscous stresses increase, inducing a higher temperature and a lower viscosity; and a higher load causes higher viscous stresses, thus the higher friction loss. Three initial temperatures are chosen to calculate the power loss due to friction, as we can see in Fig. 14(a). These results reveal that the frictional power loss increases with decreased fluid viscosity and rising temperature.

In order to compare our model and methodology with published works [12], which principally focused on the impact of α_L, which is the difference between piston and cylinder length, are considered and used for the calculation of the friction power loss. The results for three different α_L values are shown in Fig. 14(b). From this result, it can be seen that the by reducing α_L from 1 to 0.25, the maximum value of friction power loss decrease by 19 W between 0° and 180° and by 9 W between 180° and 360° degrees, while results in [12] are approximatively 3 W and 2 W, respectively. This difference in value can be justified by the heat effect considered in our model. In the same way, Fig. 14(c) shows the evolution of the lost power as a function of external pressure. It is proportional to the external forces applied. In general, the friction power loss has a large value during the loading period (between 0° and 180°), which can also be confirmed from [8,12].

This paper provides an in-depth TEHD model to study axial piston pumps' piston/cylinder interface. Important parameters involved in the efficiency loss mechanism of the piston/cylinder interface, such as the

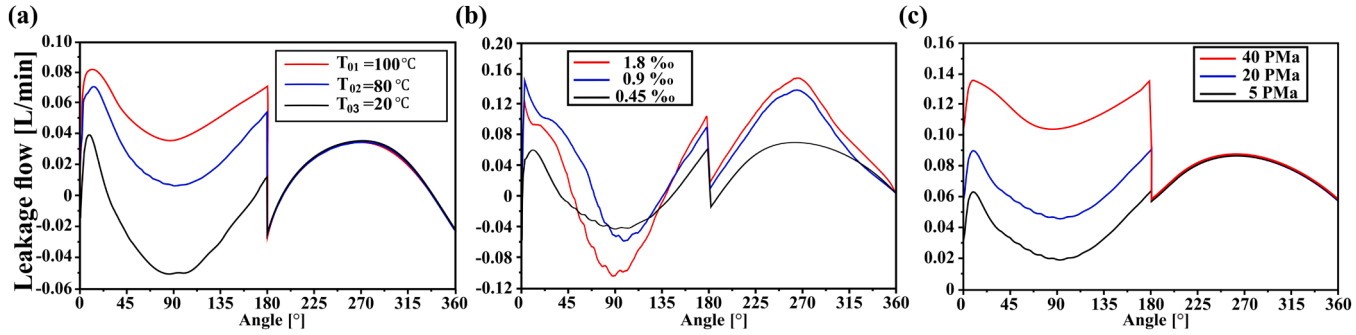

Fig. 13. Leakage flow with a fixed shaft speed at 1200 rpm for a single piston: (a) for different values of temperature, (b) for different values of piston clearance, and (c) for different values of the applied load.

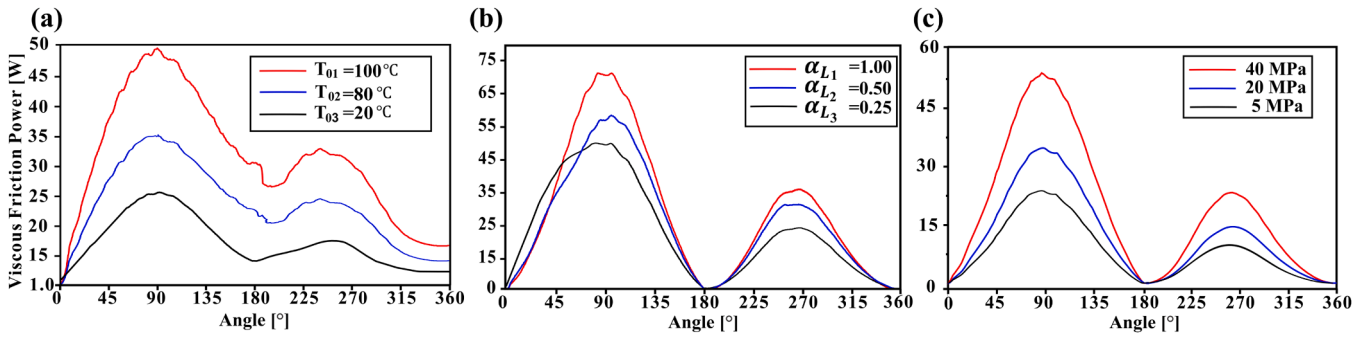

Fig. 14. Frictional power loss: (a) for different values of temperature, (b) different values of piston and cylinder length difference ratio, and (c) different values of the applied load Conclusions.

friction forces, leakage flow and energy loss, are computed and analysed under different operating conditions.

For a certain shaft rotation angle of the typical case (rotational speed of 3000 RPM and a load of 40 MPa), the film thickness and pressure differences can vary up to 8 μm and 24 MPa. By comparing the results with and without elastic deformation of the solid interface, the film thickness and the pressure increase by 5% and 20%, respectively. Thermal effects on flow are critical where the decrease in fluid viscosity of 0.03 Pa.s leads to an immediate boost of 0.08 L/min.

The increase in temperature between the piston and the cylinder leads to a rise in viscous frictional forces. By varying the initial temperature of the fluid from 40 to 55 ℃, the maximum value of axial friction force increases up to almost double the initial value. The friction forces decrease by increasing the rational speed or decreasing the load.

The loss of viscous friction varies proportionally with the temperature, the external pressure and the distance between the end of the piston and the bottom of the cylinder, respectively. The lost power reaches its maximum when the piston tip exits the maximum of the cylinder chamber, varying until reaching a difference of 19 W in the high-pressure zone and 9 W in the discharge zone.

The effects of heat exchange on the elastic deformation of solid bodies are not excluded in our research. The comparison between elastic deformation with and without temperature effects is analysed. Setting the temperature at 41 °C, the results reveal that the elastic deformation of the piston increases by 2.2 μmwhile that of the cylinder increases by 8 μm. This shows that the thermal effect can influence the film dynamics strongly.

From the results of this work, some suggestions to improve the APPs design and lifespan can be summarised as follows: the use of new materials alloys with a high capacity of absorbing heat and minor deformation for manufacturing pistons will help to reduce the heat transfer in the pressure line between the piston and cylinder block in APP. The consideration of temperature effects in predicting the lubrication mechanism of the piston/cylinder interface is more realistic to the normal working condition of the pump. The TEHD does not only import the effects of flow or elastic deformation but directly the power of the pump. It is important to point out that the methodology used in this work, particularly for solving Reynolds' equation and energy equation, can be applied to other APPs lubricating interfaces such as slipper/swashplate and cylinder/valve plate. The employed analysis and FVM will remain the same despite the geometric differences.

Originality and acknowledgement

We declare that we have written entirely original work; it has not been published or presented elsewhere in part or entirety and is not considered by another journal.

The work and/or words of others used in this manuscript have been appropriately cited and quoted.

Declaration of Competing Interest

The authors declare that they have no known competing financial interests or personal relationships that could have appeared to influence the work reported in this paper.

Data Availability

Data will be made available on request.

Acknowledgements

This work was supported by the Key Research and Development Program of Zhejiang Province (grant number 2022C01139); and the Key Research and Development Program of Zhejiang Province (grant number 2020C01153).

References

[1] Chao Q, Zhang J, Xu B, Huang H, Pan M. A review of high-speed electro-hydrostatic actuator pumps in aerospace applications: challenges and solutions. J Mech Des 2019;Vol. 141(No. 5):050801. https://doi.org/10.1115/1.4041582.
[2] Zhang J, Xu H, Chen J, Huang W, Huang X, Lyu F, et al. Modeling and analysis of the tilt behavior of the cylinder block in a high-speed axial piston pump. Mech Mach Theory 2022;Vol. 170:104735. https://doi.org/10.1016/j.mechmachtheory.2022.104735.
[3] Ivantysynova M, Lasaar R. An investigation into micro- and macrogeometric design of piston/cylinder assembly of swash plate machines. Int J Fluid Power 2004;Vol. 5 (No. 1):23–36. https://doi.org/10.1080/14399776.2004.10781181.
[4] Chen Y, Zhang J, Xu B, Chao Q, Liu G. Multi-objective optimisation of micron-scale surface textures for the cylinder/valve plate interface in axial piston pumps. Tribol Int 2019;Vol. 138:316–29. https://doi.org/10.1016/j.triboint.2019.06.002.
[5] Ernst M, Vacca A, Ivantysynova M, Enevoldsen G. Tailoring the Bore surfaces of water hydraulic axial piston machines to piston tilt and deformation. Energies 2020;Vol. 13(No. 22):5997. https://doi.org/10.3390/en13225997.
[6] Zhang J, Lyu F, Xu B, Huang W, Wu W, Guo Z, et al. Simulation and experimental investigation on low wear rate surface contour of piston/cylinder pair in an axial piston pump. Tribol Int 2021;Vol. 162:107127. https://doi.org/10.1016/j.triboint.2021.107127.
[7] Lyu F, Zhang J, Sun G, Xu B, Pan M, Huang X, et al. Research on wear prediction of piston/cylinder pair in axial piston pumps. Wear 2020;Vols. 456–457:203338. https://doi.org/10.1016/j.wear.2020.203338.
[8] Jiang J, Wang K, Yan W, Sun Y. A novel fluid structure interaction model for the grooved piston-cylinder interface in axial piston pump. AIP Adv 2019;Vol. 9(No. 5):055013. https://doi.org/10.1063/1.5090596.
[9] Ransegnola T, Shang L, Vacca A. A study of piston and slipper spin in swashplate type axial piston machines. Tribol Int 2021:107420. https://doi.org/10.1016/j.triboint.2021.107420.
[10] Schuhler G, Jourani A, Bouvier S, Perrochat J-M. Efficacy of coatings and thermochemical treatments to improve wear resistance of axial piston pumps. Tribol Int 2018;Vol. 126:376–85. https://doi.org/10.1016/j.triboint.2018.05.007.
[11] Shang L, Ivantysynova M. Scaling criteria for axial piston machines based on thermo-elastohydrodynamic effects in the tribological interfaces. Energies 2018;Vol. 11(No. 11):3210. https://doi.org/10.3390/en11113210.
[12] Zhao B, Hu X, Li H, Liu Y, Zhang B, Dong Q. A new approach for modeling mixed lubricated piston-cylinder pairs of variable lengths in swash-plate axial piston pumps. Materials 2021;Vol. 14(No. 19):5836. https://doi.org/10.3390/ma14195836.
[13] Pelosi M, Ivantysynova M. The impact of axial piston machines mechanical parts constraint conditions on the thermo-elastohydrodynamic lubrication analysis of

the fluid film interfaces. Int J Fluid Power 2013;Vol. 14(No. 3):35–51. https://doi.org/10.1080/14399776.2013.10801412.
[14] Chen X, Li F, Haidak G, Wang D, Li S. Characterisations of the oil film considering the elastohydrodynamic lubrication effect of the PIston–cylinder interface. AIP Adv 2020;Vol. 10(No. 9):095017. https://doi.org/10.1063/5.0019610.
[15] Wang D, Song Y, Tian J, E S, Haidak G. Research on the fluid film lubrication between the piston-cylinder interface. AIP Adv 2018;Vol. 8(No. 10):105330. https://doi.org/10.1063/1.5064382.
[16] Pelosi M, Ivantysynova M. A novel fluid-structure interaction model for lubricating gaps of piston machines. Presented at the FLUID STRUCTURE INTERACTION 2009. Roual Mare Village Crete 2009.
[17] Song Y, Ma J, Zeng S. A numerical study on influence of temperature on lubricant film characteristics of the Piston/Cylinder interface in axial piston pumps. Energies 2018;Vol. 11(No. 7):1842. https://doi.org/10.3390/en11071842.
[18] Nie S, Guo M, Yin F, Ji H, Ma Z, Hu Z, et al. Research on fluid-structure interaction for piston/cylinder tribopair of seawater hydraulic axial piston pump in deep-sea environment. Ocean Eng 2021;Vol. 219:108222. https://doi.org/10.1016/j.oceaneng.2020.108222.
[19] Jeong H-S, Kim H-E. On the instantaneous and average piston friction of swash plate type hydraulic axial piston machines. KSME Int J 2004;Vol. 18(No. 10):1700–11. https://doi.org/10.1007/BF02984318.
[20] Cervelin L, Flesch CA, Flesch RCC, Scussel JN, Penz CA. Measurement of the friction forces between piston and cylinder in reciprocating machines using the connecting rod strain behavior. Mech Syst Signal Process 2019;Vol. 130:677–91. https://doi.org/10.1016/j.ymssp.2019.05.026.
[21] Ma X, Wang QJ, Lu X, Mehta VS. Piston surface design to improve the lubrication performance of a swash plate pump. Tribol Int 2019;Vol. 132:275–85. https://doi.org/10.1016/j.triboint.2018.12.023.
[22] Manring ND. Friction forces within the cylinder bores of swash-plate type axial-piston pumps and motors. J Dyn Syst Meas Control 1999;Vol. 121:531–7. https://doi.org/10.1115/1.2802507.
[23] Ma X, Wang QJ, Lu X, Mehta VS. A transient hydrodynamic lubrication model for Piston/Cylinder interface of variable length. Tribol Int 2018;Vol. 118:227–39. https://doi.org/10.1016/j.triboint.2017.09.035.
[24] Bergada JM, Kumar S, Davies D, Ll, Watton J. A complete analysis of axial Piston pump leakage and output flow ripples. Appl Math Model 2012;Vol. 36(No. 4):1731–51. https://doi.org/10.1016/j.apm.2011.09.016.
[25] Kumar S, Bergada JM. The effect of piston grooves performance in an axial piston pumps via CFD analysis. Int J Mech Sci 2013;Vol. 66:168–79. https://doi.org/10.1016/j.ijmecsci.2012.11.005.
[26] Qian D, Liao R, Xiang J, Sun B, Wang S. Thermal fluid–structure interaction analysis on the piston/cylinder interface leakage of a high-pressure fuel pump for diesel engines. Proc Inst Mech Eng Part J: J Eng Tribol 2017;Vol. 231(No. 6):791–8. https://doi.org/10.1177/1350650116679266.
[27] Li F, Wang D, Lv Q, Haidak G, Zheng S. Prediction on the lubrication and leakage performance of the piston–cylinder interface for axial piston pumps. Proc Inst Mech Eng Part C: J Mech Eng Sci 2019. https://doi.org/10.1109/ACCESS.2019.2919493.
[28] Pelosi M, Ivantysynova M. Heat transfer and thermal elastic deformation analysis on the piston/cylinder interface of axial piston machines. J Tribol 2012;Vol. 134(No. 4):041101. https://doi.org/10.1115/1.4006980.
[29] Haidak Gaston, Dongyun Wang, Shiju E, Feiyue Li. The impact of the deformation phenomenon on the process of lubricating and improving the efficiency between the slipper and swashplate in axial piston machines. IEEE Access 2019.
[30] Schenk A, Ivantysynova M. A transient thermoelastohydrodynamic lubrication model for the slipper/swashplate in axial piston machines. J Tribol 2015;Vol. 137(No. 3):031701. https://doi.org/10.1115/1.4029674.
[31] Pelosi M. An investigation of the fluid-structure interaction of piston/cylinder interface. Doctoral dissertation. Perdue Univ USA 2012.
[32] Nie S, Guo M, Yin F, Ji H, Ma Z, Hu Z, et al. Research on fluid-structure interaction for piston/cylinder tribopair of seawater hydraulic axial piston pump in deep-sea environment. Ocean Eng 2021;Vol. 219:108222. https://doi.org/10.1016/j.oceaneng.2020.108222.